On the efficient and reliable numerical solution of rate-and-state friction problems

Elias Pipping, Ralf Kornhuber, Matthias Rosenau, Onno Oncken

Summary

We present a mathematically consistent numerical algorithm for the simulation of earthquake rupture with rate-and-state friction. Its main features are adaptive time-stepping, a novel algebraic solution algorithm involving nonlinear multigrid and a fixed point iteration for the rate-and-state decoupling. The algorithm is applied to a laboratory scale subduction zone which allows us to compare our simulations with experimental results.

Using physical parameters from the experiment, we find a good fit of recurrence time of slip events as well as their rupture width and peak slip. Computations in 3D confirm efficiency and robustness of our algorithm.

1. Introduction

Numerical simulations continue to grow in importance as a source of insight into earthquakes and seismic cycles. Due to observational limits, they provide a natural way to explore geological systems which are capable of producing rare but hazardous events over longer time scales. We know from laboratory experiments (Dieterich 1979) that frictional forces are strongly dependent on both the rate of sliding and material memory effects; simulations involving rate-and-state friction (Ruina 1983) are thus of particular interest.

The numerical realisation of rate-and-state friction is far from trivial, however. A few key challenges can be identified: First, rate-and-state friction models typically lead to nonlinear partial differential equations that are strongly coupled to additional state variables. Second, deformation rates cover a considerable range: In nature, over ten orders of magnitude lie between the plate convergence velocity and typical rupture velocities. This makes adaptive, unconditionally stable time-stepping indispensable. And third, such unconditionally stable time stepping methods typically require the solution of a large-scale, nonlinear algebraic problem in each time step. This necessitates the use of locally refined grids and fast multigrid solvers, in particular in three space dimensions.

Numerical simulations of earthquake rupture started in the 1970s (Andrews 1976; Das et al. 1977) with a variety of methodological developments since (Cochard et al. 1994; Geubelle et al. 1995; de la Puente et al. 2009) only to mention a few.

Past developments involving rate-and-state friction include the use of boundary element methods which are well-suited for homogeneous problems (Perrin et al. 1995; Lapusta et al. 2000; Lapusta et al. 2009; Kaneko et al. 2010; Barbot et al. 2012), spectral elements (Kaneko et al. 2008) and discontinuous Galerkin for a regularised model (Pelties et al. 2014) as spatial discretisation schemes. To discretise in time, implicit methods have already been employed on a few occasions (Pelties et al. 2014) and in addition to adaptivity (Liu et al. 2005), a physically motivated step size control has seen repeated use (Lapusta et al. 2000; Lapusta et al. 2009; Kaneko et al. 2010; Barbot et al. 2012)

These approaches have successfully reproduced a rich spectrum of earthquake and slow-slip-related behaviour (Liu et al. 2005; Lapusta et al. 2009) or spatial, temporal variations of seismic slip evolution on seismogenic faults (Lapusta et al. 2000; Kato 2004; Kaneko et al. 2010; Kato 2014), and fast velocity-weakening (Ampuero et al. 2008) demonstrating the strengths of the strategies applied.

Past developments have not, however, attempted to appropriately resolve the mathematical coupling intrinsic to the rate-and-state components of the constitutive law. Merging algebraic solution with discretisation, only a fixed number of updates is applied and accuracy is regulated by adapting the corresponding time step (Perrin et al. 1995; Kaneko et al. 2008; Pelties et al. 2014).

In this article, we present a novel solver for the numerical simulation of viscoelastic deformation subject to rate-and-state friction as it occurs, e.g. in subduction zones. The solver is mathematically consistent in the sense that it resolves the rate-and-state coupling up to any prescribed tolerance. Its main features are: Adaptive time-stepping based on an implicit Newmark scheme (Newmark 1959) to resolve almost instantaneous slip events; finite elements with local mesh refinement guided by predefined seismogenic zones to resolve complex geometries and spatial heterogeneities; a fast, reliable algebraic solution procedure involving a fixed-point iteration (Pipping et al. 2013; Pipping 2014) and a non-smooth Newton multigrid solver (Gräser 2011; Pipping 2014; Gräser et al. 2016).

The efficiency and reliability of our numerical solver and in particular the interplay of the fixed-point iteration with adaptive time-stepping is demonstrated through numerical sample computations. We validate our algorithm through a comparison of 2D simulations of a laboratory-scale subduction zone setting with experimental results, similar to (Corbi et al. 2013; van Dinther et al. 2013). The experimental results are obtained through analogue modelling (Rosenau et al. 2009; Rosenau et al. 2010). Computations in three space dimensions indicate the potential of our approach for future real-world simulations.

2. Mathematical model and numerical solver

Equations of motion

We consider a linearly viscoelastic Kelvin-Voigt body that slides on top of a rigid foundation, subject to rate-and-state friction. To obtain a mathematical model, we introduce the tensors of viscosity and elasticity $\boldsymbol{\mathcal{A}}$ and $\boldsymbol{\mathcal{B}}$ and take the foundation as a frame of reference. We can then eliminate stress from the momentum balance equation to obtain the initial value problem

$$\nabla \cdot \left[\boldsymbol{\mathcal{A}}\boldsymbol{\varepsilon}(\dot{\boldsymbol{u}}) + \boldsymbol{\mathcal{B}}\boldsymbol{\varepsilon}(\boldsymbol{u})\right] + \boldsymbol{b} = \rho\ddot{\boldsymbol{u}} \tag{1}$$

with unknown displacement $\boldsymbol{u}$ (we denote by $\boldsymbol{\varepsilon}$ the strain, by $\boldsymbol{b}$ the body forces, and by ρ the mass density). On three different parts of the boundary, we prescribe the velocity, normal forces, and rate-and-state friction.

Rate-and-state friction

By rate-and-state friction we mean here the law

$$\mu(V,\theta) = a\sinh^{-1}\left(\frac{V}{2V_\theta}\right) \quad \text{with} \quad V_\theta = V_* \exp\left(-\frac{\mu_* + b\log(\theta V_*/L)}{a}\right) \tag{2}$$

presented in (Rice et al. 1996) as a regularisation of the equation

$$\mu(V,\theta) = a\log\left(\frac{V}{V_\theta}\right) = \mu_* + a\log\frac{V}{V_*} + b\log\frac{\theta V_*}{L} \tag{3}$$

(see (Marone 1998) for a historical overview), complemented by the evolution equation

$$\dot{\theta} = 1 - \frac{\theta V}{L} \tag{4}$$

commonly referred to as the *ageing law*.

The equations (2) and (4) relate the coefficient of friction μ to the sliding velocity V and a material state variable θ. They contain two reference quantities μ_* and V_* as well as three parameters: The influence of the sliding rate is controlled by a, the state effect is controlled by b and the length L determines how quickly θ evolves in time or, in more physical terms: A sudden increase in slip velocity causes an a-fold increase in sliding friction (called the *direct velocity effect*) followed by a b-fold decrease to a new steady-state friction over a characteristic slip distance L (Scholz 1998).

In our continuum mechanical setting, a condition of the type (2) can be used to constrain the shear stress magnitude $|\boldsymbol{\sigma}_t|$ through the sliding velocity magnitude $|\dot{\boldsymbol{u}}_t|$ (as well as the normal stress σ_n and cohesion C) and vice versa by virtue of the equation

$$|\boldsymbol{\sigma}_t| = \mu(|\dot{\boldsymbol{u}}_t|,\theta)|\sigma_n| + C. \tag{5}$$

The sliding velocity vector $\dot{\boldsymbol{u}}_t$ should, moreover, be aligned with the tangential stress $\boldsymbol{\sigma}_t$, which is to say

$$-|\dot{\boldsymbol{u}}|\boldsymbol{\sigma}_t = |\boldsymbol{\sigma}_t|\dot{\boldsymbol{u}}. \tag{6}$$

Under sufficient pressure, finally, it can be assumed that no normal displacement occurs (neither penetration nor separation), so that we can completely determine $\dot{\boldsymbol{u}}$ from $\boldsymbol{\sigma}_t$ and need not distinguish between the velocity vector $\dot{\boldsymbol{u}}$ and its tangential component $\dot{\boldsymbol{u}}_t$. We can thus simply write $|\dot{\boldsymbol{u}}|$ for the sliding rate V.

By combining the assumptions (5) and (6) and extending them in a natural way to the case where $\dot{\boldsymbol{u}} = 0$ (so that $\dot{\boldsymbol{u}}$ does not have a direction), we obtain

$$-\boldsymbol{\sigma}_t = \frac{\mu(|\dot{\boldsymbol{u}}|,\theta)|\sigma_n| + C}{|\dot{\boldsymbol{u}}|}\dot{\boldsymbol{u}} \qquad \text{if } \dot{\boldsymbol{u}} \neq 0 \tag{7}$$

$$|\boldsymbol{\sigma}_t| \leq C \qquad \text{if } \dot{\boldsymbol{u}} = 0. \tag{8}$$

To summarise, we require

$$\dot{\boldsymbol{u}} \cdot \boldsymbol{n} = 0 \tag{9}$$

$$\begin{aligned} -\boldsymbol{\sigma}_t &= \frac{\mu(|\dot{\boldsymbol{u}}|,\theta)|\sigma_n| + C}{|\dot{\boldsymbol{u}}|}\dot{\boldsymbol{u}} && \text{if } \dot{\boldsymbol{u}} \neq 0 \\ |\boldsymbol{\sigma}_t| &\leq C && \text{if } \dot{\boldsymbol{u}} = 0 \end{aligned} \tag{10}$$

$$\dot{\theta} = 1 - \frac{\theta|\dot{\boldsymbol{u}}|}{L} \tag{11}$$

on the contact surface, where $\boldsymbol{n}$ denotes the outer normal.

Numerical solver

We interpret (1) and (10) in a weak sense to obtain a variational formulation of the displacement equation (see, e.g., Kikuchi et al. 1988, Sections 2.5, 10.2 or 10.3). The displacement equation can then be written as

$$\ell = \mathcal{M}\ddot{\boldsymbol{u}} + \mathcal{C}\dot{\boldsymbol{u}} + \mathcal{K}\boldsymbol{u} + Dj^{(\theta)}(\dot{\boldsymbol{u}}) \tag{12}$$

with the linear operators $\mathcal{M}$, $\mathcal{C}$, and $\mathcal{K}$ representing mass, viscosity and elasticity (the use of operators in place of bilinear forms is justified, e.g., in Rudin 1973, Chapter 12), a linear functional ℓ representing external forces, and the derivative $Dj^{(\theta)}$ of a nonlinear functional $j^{(\theta)}$ representing friction. More precisely, this functional is given by a boundary integral

$$j^{(\theta)}(\dot{\boldsymbol{u}}) = \int_{\Gamma_C} \left[\int_0^{|\dot{\boldsymbol{u}}|} \mu(v,\theta)|\sigma_n| + C \,\mathrm{d}v \right] \mathrm{d}\Gamma_C \tag{13}$$

over a state-dependent dissipation potential along the prescribed contact surface Γ_C. This abstract reformulation of (1) and (10) allows to use convexity in the construction of fast nonlinear multigrid solvers after discretisation (Pipping et al. 2013; Pipping 2014).

Our numerical routine proceeds as follows: We use an implicit Newmark scheme (Newmark 1959) to discretise (12) in time and piecewise affine finite elements to discretise in space. The resolution of the finite element mesh is controlled through the distance from the seismogenic zone by means of successive local refinement (see figures 2 and 8 below).

The time step is self-adaptively chosen by a simple step doubling strategy. More precisely, coarsening is performed by comparing the approximation of the state field resulting from two steps with a given time step size τ and the approximation resulting from one step with the step size 2τ. If the distance of these two approximations falls below a threshold δ then the new guess for the time step is 2τ. This process is repeated until the distance of two such approximations exceeds δ. If no coarsening takes place then refinement is performed in a similar fashion. The distance between two states θ and $\tilde{\theta}$ is measured by the dimensionless quantity

$$d(\tilde{\theta},\theta) = \frac{1}{|\Gamma_C|^{1/2}} \left(\int_{\Gamma_C} \left(\log \frac{\tilde{\theta}}{\theta} \right)^2 \right)^{1/2} \tag{14}$$

which is a scaled L^2 norm of the difference of the transformations $\alpha = \log(\theta V_*/L)$ and $\tilde{\alpha} = \log(\tilde{\theta} V_*/L)$. Note that this transformation is motivated by mathematical analysis in (Pipping et al. 2013).

Discretisation in time and space leaves us with a sequence of spatial problems

$$\begin{aligned} \underline{\boldsymbol{b}}_n + \underline{\mathcal{M}}\big(\frac{2}{\tau_n}\underline{\dot{\boldsymbol{u}}}_{n-1} + \underline{\ddot{\boldsymbol{u}}}_{n-1}\big) - \underline{\mathcal{K}}\big(\underline{\boldsymbol{u}}_{n-1} + \frac{\tau_n}{2}\underline{\dot{\boldsymbol{u}}}_{n-1}\big) \\ = \left(\frac{2}{\tau_n}\underline{\mathcal{M}} + \underline{\mathcal{C}} + \frac{\tau_n}{2}\underline{\mathcal{K}}\right)\underline{\dot{\boldsymbol{u}}}_n + D\underline{j}^{(\theta_n)}(\underline{\dot{\boldsymbol{u}}}_n) \end{aligned} \tag{15}$$

with matrices in place of operators, vectors instead of linear functionals, and time-step sizes τ_n. By assuming the sliding velocity to be constant in (11) over the course of a single time step and approximating it through $|\dot{\boldsymbol{u}}_{n-1/2}|$ with

$$\dot{\boldsymbol{u}}_{n-1/2} = \frac{\dot{\boldsymbol{u}}_{n-1} + \dot{\boldsymbol{u}}_n}{2}, \tag{16}$$

we obtain an explicitly solvable ordinary differential equation of the form

$$\dot{\theta} = 1 - \frac{\theta|\dot{\boldsymbol{u}}_{n-1/2}|}{L} \quad \text{with} \quad \theta(t_{n-1}) = \theta_{n-1} \tag{17}$$

at every basal grid node. Overall, this procedure leaves us with a state-dependent constraint (15) on the velocity $\dot{\boldsymbol{u}}$ and a velocity-dependent constraint (17) on the state θ.

The straight-forward approach of inserting the analytical solution to (17) into the velocity constraint (15), whereby θ would be eliminated, is not constructive since the resulting problem does not enjoy any convexity properties: The right-hand side of the state evolution equation (17) is not monotone with respect to the velocity $|\dot{\boldsymbol{u}}_{n-1/2}|$. In comparison with the separate problems (15) and (17), the resulting problem would thus be very difficult to solve. If we treat θ as known, instead, we obtain a solvable problem.

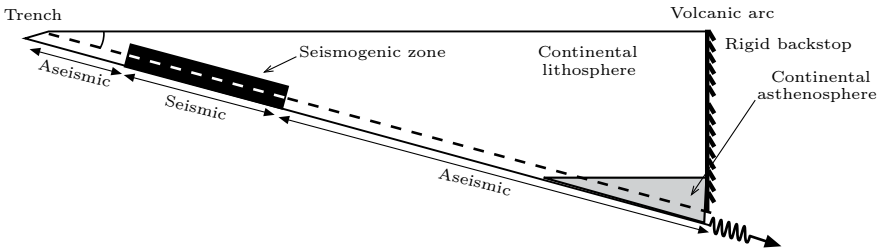

Figure 1: A subduction zone model.

The fact that θ is unknown can now be accounted for through a fixed-point iteration: Starting from a prediction θ_n^0 for the new state θ_n, we can compute a corresponding velocity $\dot{\boldsymbol{u}}_n^1$ according to (15), then compute a corresponding state θ_n^1 from (17),

$$\begin{aligned} \theta_n^{k-1} &\mapsto \dot{\boldsymbol{u}}_n^k \quad \text{via (15)} \\ \dot{\boldsymbol{u}}_n^k &\mapsto \theta_n^k \quad \text{via (17)} \end{aligned} \tag{18}$$

and continue in this manner until both quantities cease to change. More precisely, the iteration is terminated with the result θ_n^k once the stopping criterion

$$d(\theta_n^k, \theta_n^{k-1}) \leq \varepsilon \tag{19}$$

is met for given fixed point tolerance $\varepsilon > 0$.

This fixed-point approach is particularly convenient because the evaluation of the corresponding states θ_n^k can be carried out in closed form, while the velocities $\dot{\boldsymbol{u}}_n^k$ can be computed iteratively by fast and reliable truncated nonsmooth Newton multigrid methods (Gräser 2011; Gräser et al. 2009a; Gräser et al. 2013; Gräser et al. 2009b). Here, each step consists of nonlinear Gauß-Seidel smoothing (Gräser et al. 2016; Pipping 2014) and 5 steps of a standard $V(3,3)$-cycle (3 pre- and 3 postsmoothing steps) with a linear Gauß-Seidel smoother and 10 levels resulting from local adaptive refinement in the predefined seismogenic zone. The computational effort for each truncated nonsmooth Newton multigrid step thus increases linearly with the number of unknowns.

As an alternative, one could decouple rate and state by using the known vector $\dot{\boldsymbol{u}}_{n-1}$ in place of $\dot{\boldsymbol{u}}_{n-1/2}$ defined in (16). However, explicit discretisations typically suffer from instabilities that necessitate very small time steps to be made, thereby more than cancelling the benefits of the non-coupling: In the numerical experiments presented in the following section, such an explicit scheme leads to nearly twice as much computational effort as our fixed-point approach.

3. 2D simulations on the laboratory scale

3.1. Numerical simulations of seismic cycles

As a particular case of a sliding body, we now consider a laboratory-scale analogue (Rosenau et al. 2009; Rosenau et al. 2010) of a subduction zone shown in figure 1: A

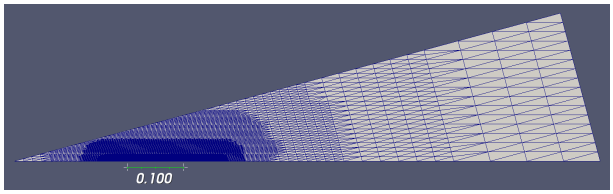

(a) Complete view.

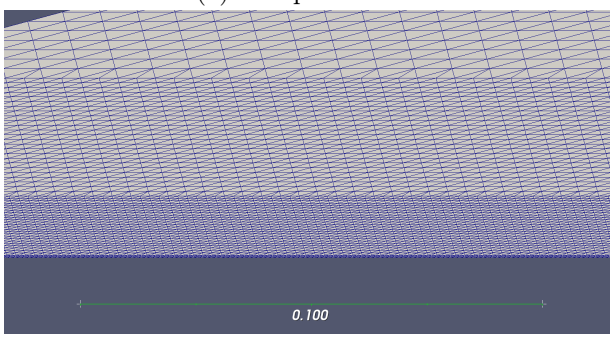

(b) Zoom into strong refinement at seismogenic zone.

Figure 2: Computational domain for 2D simulations on the laboratory scale.

wedge of viscoelastoplastic, rate-strengthening material is driven against a rigid backstop by means of a moving base.

The wedge measures 1 m in length, 27 cm in depth, and 10 cm in width (this dimension is neglected here) with a dipping angle of approximately 15°. Its lower 6 cm are particularly viscous; further up the base, a block of rate-weakening material serves as the seismogenic zone. This block is 4 cm thick (we treat this thickness as zero), measures 20 cm along the base, and ends 35 cm from the trench, measured along the surface.

For the bulk of the material, we use the Kelvin-Voigt model of viscoelasticity, as explained in the previous section. As boundary conditions, we prescribe zero traction forces on the surface, rate-and-state friction at the base, and a time dependent velocity vector $\boldsymbol{v}(t)$ that is parallel to the base at the vertical edge of the wedge. More precisely,

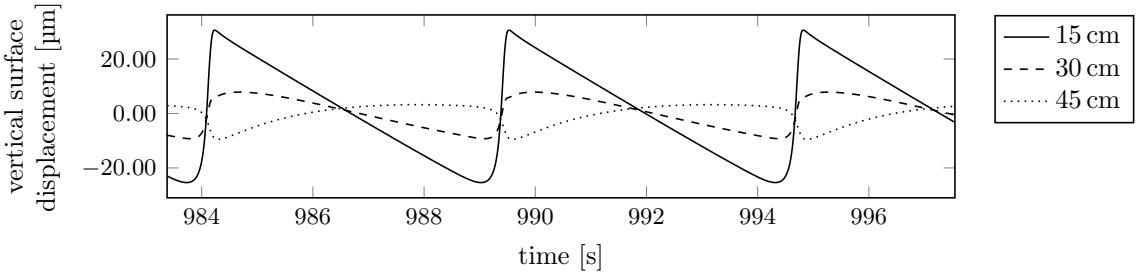

Figure 3: Vertical surface displacement relative to a time average, 15 cm, 30 cm, and 45 cm from the trench.

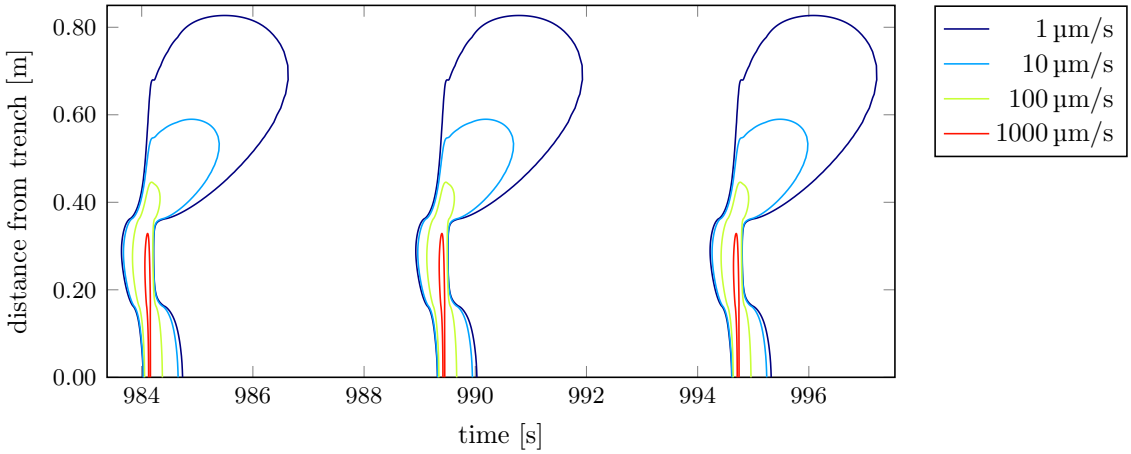

(a) Three subsequent events.

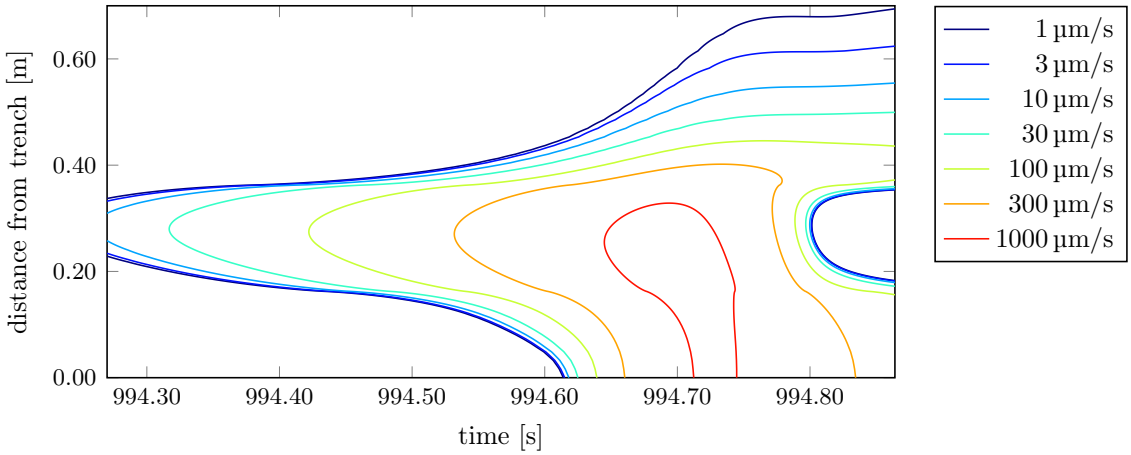

(b) Zoom into the last event.

Figure 4: Isolines of the basal slip rate relative to plate convergence.

we prescribe $|\boldsymbol{v}(t)| = \frac{1}{2}v_0(1 - \cos(\pi t/t_0))$ for $t \leq t_0$ and $|\boldsymbol{v}(t)| = v_0$ for $t \geq t_0$ with $t_0 = 100\,\mathrm{s}$ and the plate convergence velocity v_0. Note that the choice of the transient velocity for $t \leq t_0$ does not influence the behaviour for large times t as they are of interest here.

Since slip events can be expected to nucleate on the rate-weakening patch, we choose to resolve it particularly well with our computational mesh as shown in figure 2.

In order to allow for a comparison of our numerical simulation with the laboratory experiments presented in (Rosenau et al. 2009; Rosenau et al. 2010), we take parameters from the physical setup whenever available. The only exception is a smaller bulk modulus accounting for plasticity effects in our elastic material law. The unknown rate-and-state parameters have to be selected by educated guessing from the experimentally determined range of values. An overview of all material parameters is given in table 1. We note that

the computational results are rather sensitive with respect to $b - a$ and only moderately dependent on variations of a and L in the seismogenic zone. Further quantitative investigation of rate-and-state parameters will be the subject of future research.

Our simulations show the expected qualitative behaviour: The surface subsides near the trench and then rises abruptly, repeatedly and periodically. This is illustrated in figure 3, where the evolution of the vertical surface displacement relative to a time average is shown at three different points on the surface. The largest near-instantaneous upward motion is observed above the seismogenic zone (15 cm). Less pronounced displacement occurs further from the trench, first in the same direction (30 cm) and finally in the opposite, downward direction (45 cm).

A different perspective is taken in figure 4, which shows how the the slip rate evolves in time along the base. More precisely, figure 4a shows four isolines of the difference between the basal slip rate and plate convergence in the space time plane. We identify three perfectly periodic slip events, which nucleate in the seismogenic zone, spread out, and produce considerable afterslip in the rate-strengthening areas. The last of the three events is shown again in detail in figure 4b, over a time interval of approximately 0.5 s. Note that the experimental resolution in (Rosenau et al. 2009; Rosenau et al. 2010) was limited to one measurement per second and thus less than a single measurement within this period of time.

3.2. Comparison with experimental results

For a comparison of our numerical simulation with the laboratory measurements presented in (Rosenau et al. 2009; Rosenau et al. 2010), we collect statistical data from the experiment (with 50 events) and from the simulation (with 79). Apart from a few events that occur as the wedge passes through an initial transition period from stable loading to unstable sliding, there is no variability in the simulation — we see the same seismic cycle over and over again. This parallels the experimentally observed events, which, too, show little variation in frequency and magnitude.

In figure 5, experiment and simulation are compared through boxplots of three different quantities: From left to right, we consider recurrence time, rupture width, and peak slip. For the simulation, each box essentially reduces to a single bar because of the strong

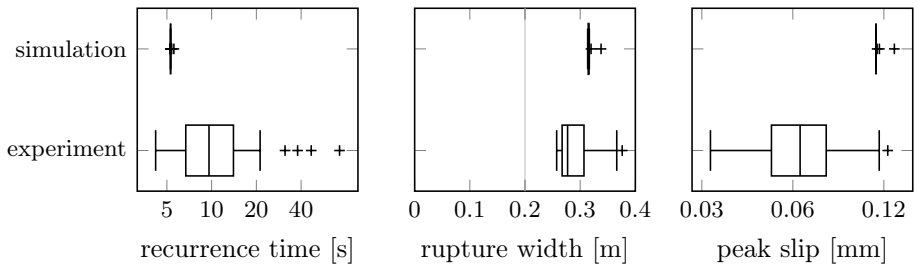

Figure 5: Comparison of simulation and experiment: Tukey boxplots for recurrence time, rupture width, and peak slip.

periodicity, with a few outliers that occur over the course of the aforementioned transition period.

The recurrence times of simulated and observed events look quite similar: Although the median in the experiment is larger than in the simulation, it is so by less than a factor of two; moreover, the simulation falls within the range of experimental observations.

Agreement of rupture widths is very good: Simulated events exceed the median of the experimental results by less than 14 % for this quantity.

Peak slip is again similar for simulated and observed events: The simulated events fall within the range of observations and the peak slip median from the experiment is exceeded by less than a factor of two.

3.3. Solver performance

We now report a few observations which illustrate the efficiency and robustness of the underlying numerical solver. We first concentrate on the performance of adaptive time-stepping, then on the fixed-point scheme (18) in combination with fast multigrid methods, and finally on some features of their interplay.

The first two plots in figure 6 show how adaptive time-stepping captures the two different time scales of a seismic cycle. We focus on the three events that were already considered in figure 4a, now illustrated by isolines of the vertical surface displacement, relative to a time average. Observe how the occurrence of an event is accompanied by the fully automatic time step size reduction of two orders of magnitude.

Our algebraic solver consists of an (outer) fixed-point iteration (18) in combination with (inner) multigrid iterations. The efficiency of this approach is illustrated in the final two plots of figure 6. Here, we show the number of required (outer) fixed-point iterations and the total number of (inner) multigrid iterations for each of the spatial problems. Observe that the required number of outer and inner iterations remains essentially constant over the entire time span: No more than five (outer) fixed-point iterations involving no more than a total of 16 (inner) multigrid steps are necessary to solve any of the spatial problems up to discretisation accuracy, even across multiple seismic cycles.

This kind of efficiency stems not only from the good convergence properties of the iterative algebraic solution procedure but also from a proper choice of the stopping criterion. We terminate the iteration once the difference of two subsequent iterates falls below a prescribed error tolerance ε. The optimal choice can be expected to be of the same order as the adaptive time-stepping tolerance, so that we choose them identical and equal to $\varepsilon = 10^{-5}$. An overly large tolerance would lead to just a single algebraic solution step and thus a simple predictor-corrector scheme but also require a significant reduction of the time step size in order to preserve the overall accuracy. A very small tolerance instead would cause additional fixed-point iterations to be made without an improvement of the overall accuracy, which would then be limited by the temporal discretisation error. These considerations are confirmed in figure 7, which shows the computational effort in terms of the overall number of multigrid steps over the prescribed error tolerance. A fixed point tolerance of about $\varepsilon = 10^{-4}$ appears to be optimal which turns out to be close to the selected tolerance $\varepsilon = 10^{-5}$ taken from the adaptive time stepping procedure

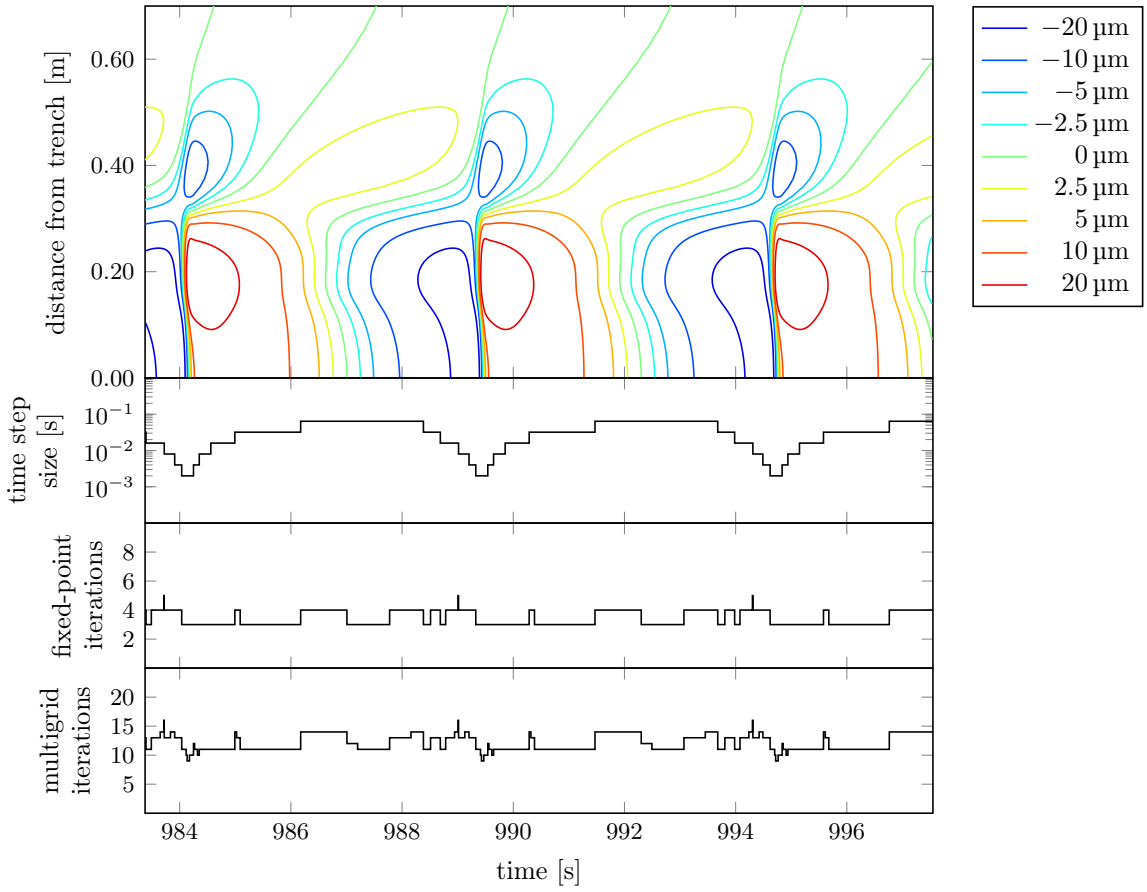

Figure 6: From top to bottom: Vertical surface displacement (relative to a time average), time step size, outer fixed-point iterations and total number of inner multigrid iterations for each of the spatial problems.

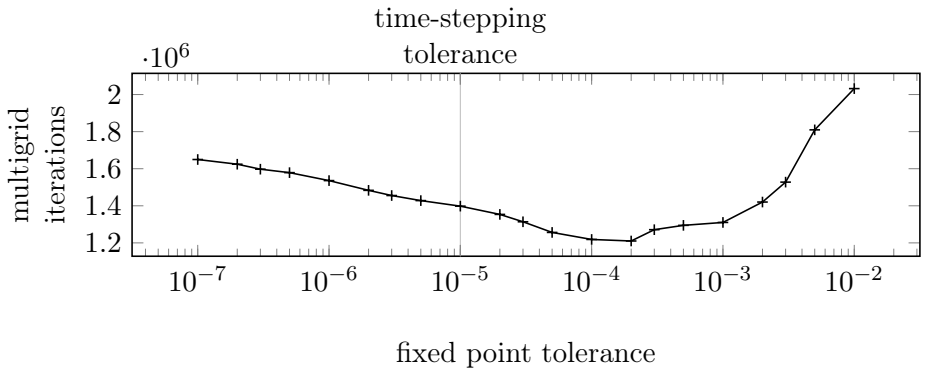

Figure 7: Computational effort (in terms of the total number of multigrid iterations) over the prescribed error tolerance ε.

as mentioned above.

4. 3D simulations

4.1. Numerical simulations of seismic cycles

To test our methodology in a three-dimensional setting, we consider the subduction zone geometry from figure 1 again, but now increase its width from 10 cm to 60 cm. As a consequence, lateral effects can no longer be neglected. For the seismogenic zone, we introduce a trapezoidal patch starting at the same distance from the trench as in the 2D model, but now with a length of 15 cm on one side and 25 cm on the other. The trapezoidal shape is chosen in order to stabilise the point of nucleation.

In light of limited computational resources, we select a rather coarse spatial mesh with 51811 unknowns and cell diameters ranging from 0.5 cm to 30 cm as illustrated in figure 8. Nevertheless, convergence tests confirm that the corresponding accuracy already allows for qualitatively correct simulation results.

Figure 9 shows spatial isolines of the difference between the basal slip rate and plate convergence along the seismogenic zone (whose outlines are shown in grey) during one seismic event. The different figures represent different snapshots, each taken 30 time steps after the other, starting from the first frame at approximately 991 s until the last frame approximately 0.46 s later. We see here how rupture nucleates on the boundary of the domain, accelerates and grows towards its center, where it is finally arrested.

4.2. Solver performance

The performance of the numerical solver is essentially the same as in the 2D case. The topmost plot in figure 10 illustrates the adaption of the time step to the final three slip events of the simulation. Note that, just like in the 2D case, the simulation shows perfectly periodic behaviour. The two lower plots in figure 10 show that the number of outer fixed-point iterations remains essentially the same as in the 2D case.

5. Conclusion

We have presented a novel solution algorithm for the numerical simulation of viscoelastic deformation subject to rate-and-state friction in two and three space dimensions. Our numerical approach is not only fast (because it adapts to the temporal and spatial spacels of the problem) and robust (because a potential underresolution of algebraic problems is automatically compensated through a smaller time step size) but also flexible enough to allow for material heterogeneities, complex geometries, and future incorporation of additional sources of non-smoothness like contact or plasticity.

Application to a laboratory scale subduction zone provided quantitative agreement of 2D simulations with experiments. A qualitative comparison of our approach with published studies shows that our algorithm has good potential to capture a range of kinematic behaviours associated to the seismic cycle along various parts of the plate

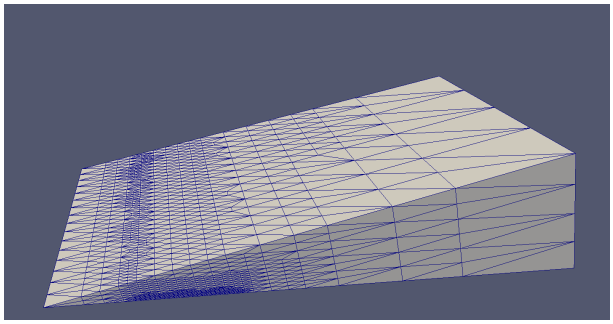

(a) Complete view.

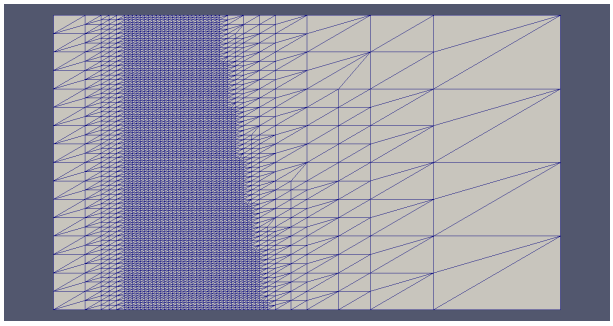

(b) View from below, with strongly refined seismogenic zone.

Figure 8: Computational domain for 3D simulations.

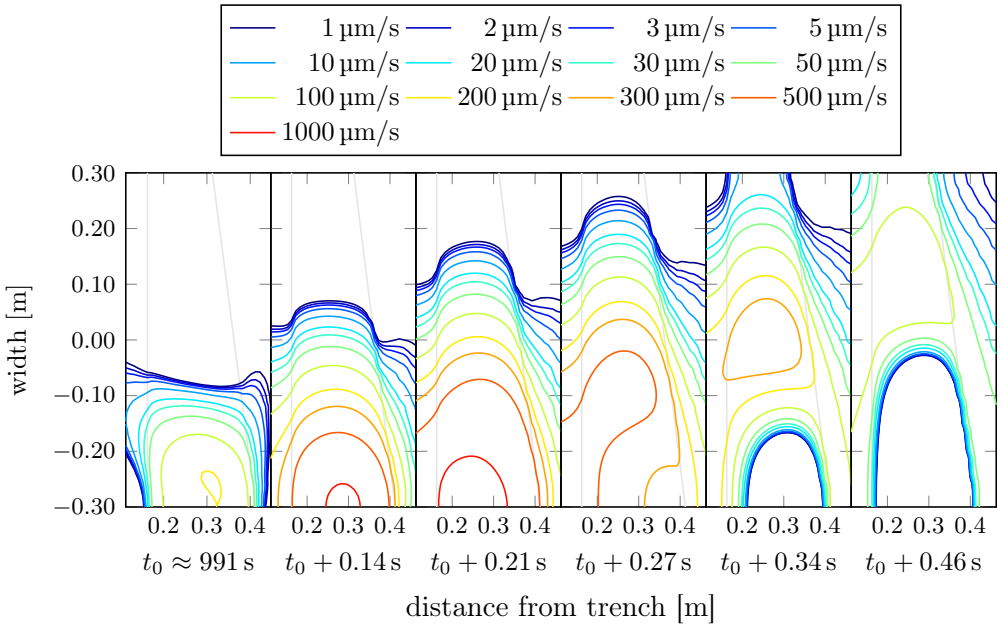

Figure 9: Spatial isolines of the basal slip rate relative to plate convergence at consecutive instants of time.

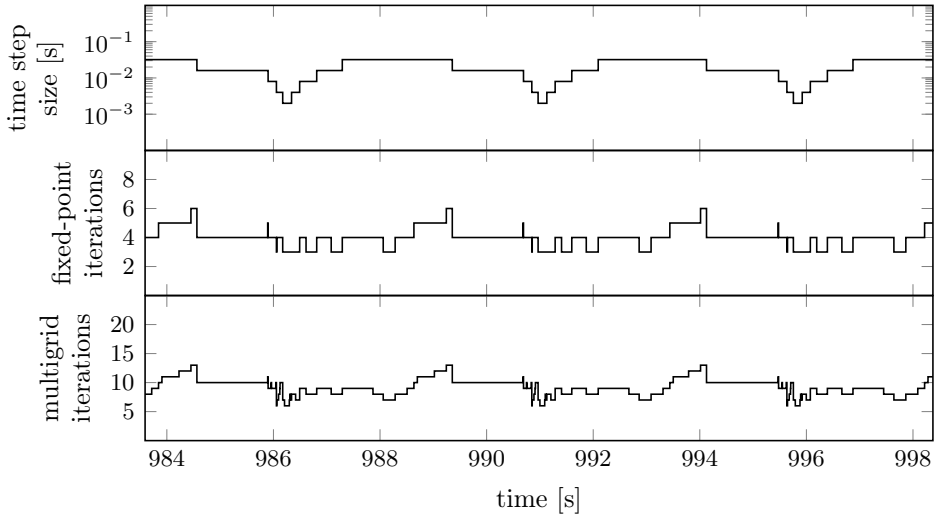

Figure 10: Number of fixed-point iterations in relation to the adaptive time-step size.

interface contact: We identify slip acceleration preceding the main rupture as shown in several other studies (Liu et al. 2005), decaying afterslip focused below the downdip end of coupling, or lateral excitation of slip events in 3D.

A. Acknowledgements

This work was carried out in project B01 of the CRC 1114 supported by the German Research Foundation.

References

Ampuero, J.-P. and Y. Ben-Zion (2008). "Cracks, pulses and macroscopic asymmetry of dynamic rupture on a bimaterial interface with velocity-weakening friction". In: *Geophysical Journal International* 173.2, pp. 674–692. DOI: 10.1111/j.1365-246X.2008.03736.x.

Andrews, D. J. (1976). "Rupture velocity of plane strain shear cracks". In: *Journal Geophysical Research* 81.32, pp. 5679–5687. DOI: 10.1029/JB081i032p05679.

Barbot, S., N. Lapusta, and J.-P. Avouac (2012). "Under the Hood of the Earthquake Machine: Toward Predictive Modeling of the Seismic Cycle". In: *Science* 336.6082, pp. 707–710. DOI: 10.1126/science.1218796.

Cochard, A. and R. Madariaga (1994). "Dynamic faulting under rate-dependent friction". In: *pure and applied geophysics* 142.3–4, pp. 419–445. DOI: 10.1007/BF00876049.

Table 1: Material parameters.

Parameter		Unit	Simulation	Experiment
Gravitational acceleration		m/s	9.81	9.81
Bulk modulus		MPa	0.05	0.10
Poisson's ratio			0.3	unknown
Viscosity, upper region		kPa s	1	unknown
Viscosity, lower region		kPa s	10	10
Mass density ρ, upper region		kg/m^3	900	900
Mass density ρ, lower region		kg/m^3	1000	1000
Cohesion C		Pa	10	10
Friction	L	µm	22.5	unknown
	V_*	µm/s	50	50
	μ_*		0.7	variable[a]
	a, unstable		0.002	unknown[b]
	a, stable		0.020	unknown[c]
	$b-a$, unstable		0.015	0.015
	$b-a$, stable		-0.015	variable[d]
Plate convergence velocity v_0		µm/s	50	50
Experiment duration T		s	1000	1000

[a] From 0.7 in the bulk to 0.8 in the seismogenic zone.
[b] Known upper bound: 0.002.
[c] Order of magnitude: 0.010 to 0.020.
[d] Order of magnitude: -0.020 to -0.010.

Corbi, F. et al. (2013). "The seismic cycle at subduction thrusts: 1. Insights from laboratory models". In: *Journal of Geophysical Research: Solid Earth* 118.4, pp. 1483–1501. DOI: 10.1029/2012JB009481.

Das, S. and K. Aki (1977). "A numerical study of two-dimensional spontaneous rupture propagation". In: *Geophysical Journal International* 50.3, pp. 643–668. DOI: 10.1111/j.1365-246X.1977.tb01339.x.

Dieterich, J. H. (1979). "Modeling of Rock Friction: 1. Experimental Results and Constitutive Equations". In: *Journal of Geophysical Research: Solid Earth* 84.B5, pp. 2161–2168. DOI: 10.1029/JB084iB05p02161.

van Dinther, Y. et al. (2013). "The seismic cycle at subduction thrusts: 2. Dynamic implications of geodynamic simulations validated with laboratory models". In: *Journal of Geophysical Research: Solid Earth* 118.4, pp. 1502–1525. DOI: 10.1029/2012JB009479.

Geubelle, P. H. and J. R. Rice (1995). "A spectral method for three-dimensional elastodynamic fracture problems". In: *Journal of the Mechanics and Physics of Solids* 43.11, pp. 1791–1824. DOI: 10.1016/0022-5096(95)00043-I.

Gräser, C. (2011). "Convex minimization and phase field models". Dissertation. Freie Universität Berlin. URN: urn:nbn:de:kobv:188-fudissthesis000000025553-5.

Gräser, C. and R. Kornhuber (2009a). "Multigrid methods for obstacle problems". In: *Journal of Computational Mathematics* 27.1, pp. 1–44.

Gräser, C., R. Kornhuber, and U. Sack (2013). "Time discretizations of anisotropic Allen–Cahn equations". In: *IMA Journal of Numerical Analysis* 33.4, pp. 1226–1244. DOI: 10.1093/imanum/drs043.

Gräser, C., U. Sack, and O. Sander (2009b). "Truncated Nonsmooth Newton Multigrid Methods for Convex Minimization Problems". In: *Domain Decomposition Methods in Science and Engineering XVIII*. Vol. 70. Lecture Notes in Computational Science and Engineering. Springer-Verlag, Berlin, pp. 129–136. ISBN: 978-3642026775. DOI: 10.1007/978-3-642-02677-5_12.

Gräser, C. and O. Sander (2016). "TNNMG Methods for Block-Separable Minimization Problems". In preparation.

Kaneko, Y., N. Lapusta, and J.-P. Ampuero (2008). "Spectral element modeling of spontaneous earthquake rupture on rate and state faults: Effect of velocity-strengthening friction at shallow depths". In: *Journal of Geophysical Research: Solid Earth* 113.B9. B09317. DOI: 10.1029/2007JB005553.

Kaneko, Y., J.-P. Avouac, and N. Lapusta (2010). "Towards inferring earthquake patterns from geodetic observations of interseismic coupling". In: *Nature Geoscience* 3.5, pp. 363–369. DOI: 10.1038/ngeo843.

Kato, N. (2004). "Interaction of slip on asperities: Numerical simulation of seismic cycles on a two-dimensional planar fault with nonuniform frictional property". In: *Journal of Geophysical Research: Solid Earth* 109.B12. B12306. DOI: 10.1029/2004JB003001.

– (2014). "Deterministic chaos in a simulated sequence of slip events on a single isolated asperity". In: *Geophysical Journal International* 198.2, pp. 727–736. DOI: 10.1093/gji/ggu157.

Kikuchi, N. and J. T. Oden (1988). *Contact Problems in Elasticity*. Society for Industrial and Applied Mathematics. DOI: 10.1137/1.9781611970845.

Lapusta, N. and Y. Liu (2009). "Three-dimensional boundary integral modeling of spontaneous earthquake sequences and aseismic slip". In: *Journal of Geophysical Research: Solid Earth* 114.B9. B09303. DOI: 10.1029/2008JB005934.

Lapusta, N. et al. (2000). "Elastodynamic analysis for slow tectonic loading with spontaneous rupture episodes on faults with rate- and state-dependent friction". In: *Journal of Geophysical Research: Solid Earth* 105.B10, pp. 23765–23789. DOI: 10.1029/2000JB900250.

Liu, Y. and J. R. Rice (2005). "Aseismic slip transients emerge spontaneously in three-dimensional rate and state modeling of subduction earthquake sequences". In: *Journal of Geophysical Research: Solid Earth* 110.B8. B08307. DOI: 10.1029/2004JB003424.

Marone, Ch. (1998). "Laboratory-derived friction laws and their application to seismic faulting". In: *Annual Review of Earth and Planetary Sciences* 26.1, pp. 643–696. DOI: 10.1146/annurev.earth.26.1.643.

Newmark, N. M. (1959). "A Method of Computation for Structural Dynamics". In: *Journal of the Engineering Mechanics Division* 85.3, pp. 67–94.

Pelties, C., A.-A. Gabriel, and J.-P. Ampuero (2014). "Verification of an ADER-DG method for complex dynamic rupture problems". In: *Geoscientific Model Development* 7.3, pp. 847–866. DOI: 10.5194/gmd-7-847-2014.

Perrin, G., J. R. Rice, and G. Zheng (1995). "Self-healing slip pulse on a frictional surface". In: *Journal of the Mechanics and Physics of Solids* 43.9, pp. 1461–1495. DOI: 10.1016/0022-5096(95)00036-I.

Pipping, E., O. Sander, and R. Kornhuber (2013). "Variational formulation of rate- and state-dependent friction problems". In: *Zeitschrift für Angewandte Mathematik und Mechanik. Journal of Applied Mathematics and Mechanics*. DOI: 10.1002/zamm.201300062.

Pipping, E. (2014). "Dynamic problems of rate-and-state friction in viscoelasticity". Dissertation. Freie Universität Berlin. URN: urn:nbn:de:kobv:188-fudissthesis000000098145-4.

de la Puente, J., J.-P. Ampuero, and M. Käser (2009). "Dynamic rupture modeling on unstructured meshes using a discontinuous Galerkin method". In: *Journal of Geophysical Research: Solid Earth* 114.B10. B10302. DOI: 10.1029/2008JB006271.

Rice, J. R. and Y. Ben-Zion (1996). "Slip complexity in earthquake fault models". In: *Proceedings of the National Academy of Sciences* 93.9, pp. 3811–3818. DOI: 10.1073/pnas.93.9.3811.

Rosenau, M., J. Lohrmann, and O. Oncken (2009). "Shocks in a box: An analogue model of subduction earthquake cycles with application to seismotectonic forearc evolution". In: *Journal of Geophysical Research: Solid Earth* 114.B1. B01409. DOI: 10.1029/2008JB005665.

Rosenau, M. et al. (2010). "Experimental insights into the scaling and variability of local tsunamis triggered by giant subduction megathrust earthquakes". In: *Journal of Geophysical Research: Solid Earth* 115.B9. B09314. DOI: 10.1029/2009JB007100.

Rudin, W. (1973). *Functional analysis*. McGraw-Hill Book Co., New York-Düsseldorf-Johannesburg, pp. xiii+397. ISBN: 978-0070995581.

Ruina, A. (1983). "Slip Instability and State Variable Friction Laws". In: *Journal of Geophysical Research: Solid Earth* 88.B12, pp. 10359–10370. DOI: 10.1029/JB088iB12p10359.

Scholz, Ch. H. (1998). "Earthquakes and friction laws". In: *Nature* 391.6662, pp. 37–42. DOI: 10.1038/34097.